

# Relative orbit estimation and formation keeping control of satellite formations in low Earth orbits

Guoqiang Zeng<sup>a</sup>, Min Hu<sup>b,\*</sup>, Hong Yao<sup>b</sup>

<sup>a</sup> College of Aerospace and Material Engineering, National University of Defense Technology, Changsha 410073, China

<sup>b</sup> Academy of Equipment, Beijing 101416, China

## ARTICLE INFO

### Article history:

Received 3 July 2011

Received in revised form

4 October 2011

Accepted 28 February 2012

Available online 29 March 2012

### Keywords:

Satellite formation

Relative orbital elements

Extended particle filter

Impulsive maneuver

Aerodynamic control

## ABSTRACT

A new relative orbit estimation method and practical control scheme for satellite formation keeping is developed. We present the general formation description method based on the relative orbital elements and employ the extended particle filter for the relative orbit estimation using the relative distance, elevation, and azimuth measurements. The stability of the formation configuration is analyzed in the presence of the J2 perturbation and atmospheric drag. We propose a new control scheme for formation keeping, including the triple-impulse strategy for the in-plane motion, the single-impulse maneuver for the cross-track motion, and the time-optimal aerodynamic control for the along-track separation. The full analytical fuel-optimal triple-impulse solutions are then derived, which do not cause additional along-track drift compared with the conventional dual-impulse method. Effects of the thruster errors are also analyzed. Furthermore, the time-optimal aerodynamic control law for the along-track drift is presented. Simulation results show that the relative position estimation errors are within  $2 \times 10^{-2}$  m, and that of the relative velocity estimation are within  $1 \times 10^{-4}$  m/s. Moreover, the triple-impulse strategy is simple and effective, and the along-track aerodynamic control precision is under 50 m.

© 2012 Elsevier Ltd. All rights reserved.

## 1. Introduction

Formation flying is one of the key technologies for future innovative space missions. Several small, unconnected satellites operating in a coordinated way may achieve a better performance than a monolithic satellite, and possess advantages such as increased instrument resolution, reduced cost, reconfigurability, and overall system robustness, which can in turn enhance the scientific return [1]. Several ambitious distributed spacecraft missions are currently being put in operation or planned. The PRISMA satellite, which is an on-orbit technology demonstrator for autonomous formation flying and rendezvous, was launched on 15 June, 2010 [2].

The TanDEM-X satellite was launched on 21 June, 2010 and orbited in close formation with the TerraSAR-X satellite on 15 October, 2010. The twin satellites began a routine acquisition of the digital elevation model with flexible baselines on 12 December, 2010 [3]. The F6 program of the Defense Advanced Research Projects Agency, the Terrestrial Planet Finder of the National Aeronautics and Space Administration, and the Darwin mission of the European Space Agency will all utilize the technology of formation flying.

The premier problem of formation flying control is the relative orbit estimation. In recent years, a significant amount of work has been focused on formation relative orbit estimation and relative orbit control [4,5]. How [6] has shown that the relative orbit estimation errors have a significant effect on formation control. Liu [7] considered the relative navigation for formation flying using an unscented Kalman filter (UKF) and showed that the error

\* Corresponding author. Tel.: +86 106 636 4201.

E-mail address: [songjl@mail.ustc.edu.cn](mailto:songjl@mail.ustc.edu.cn) (M. Hu).

of the relative position and velocity estimation can be estimated in the centimeter and millimeter per second scales, respectively. Xing [8] proposed the extended Kalman filter (EKF) method for relative position and attitude estimation, and Dang [9] developed a modified UKF algorithm for relative motion estimates. The original Kalman filter is widely used in relative navigation; however, its inherent linearization process typically introduces significant biases in the estimation results. A particle filter (PF) achieves a recursive Bayesian estimation via a non-parametric Monte Carlo method and shows significant advantages in the nonlinear estimation problem [10]. A way of generating the importance density function of a PF is essential to improve its performance. EKF and UKF are effective in generating the importance density function [11]. Therefore, because of the strong non-linearity of the dynamics of satellites formation flying; the extended PF (EPF) is adopted to improve the precision of the relative orbit estimation.

An accurate relative orbit control is also very important for the practical implementation of satellites formation flying. A number of effective controllers are presented in recent literature, such as the linear quadratic regulator [12], the sliding mode control [13–16], and relative orbital elements [17–20]. Kristiansen [21] reviewed the previous work on the field of spacecraft formation flying, including modeling approaches and controller design. Wang [22] designed the nonlinear controller based on a polynomial eigenstructure assignment for spacecraft precise formation flying. Sun [23] proposed a finite-time control technique for six-degrees-of-freedom spacecraft formation control. All these controllers were effective for formation control; however, with an increasing number of projects in operation, a practical formation control has also become an area of concern. Relative orbital elements were demonstrated during the GRACE, PRISMA, and TanDEM-X missions. Therefore, the current study will concentrate on formation keeping based on relative orbital elements. D'Amico and Ardaens [20] proposed a dual-impulse method for the in-plane relative control and a single-impulse control for the cross-track motion; when the control period increases, the dual-impulse maneuver causes an additional along-track drift. Hence, the use of a dual-impulse maneuver for an extended control period of formation keeping may be restricted.

As a matter of fact, for satellite formations with long periods in low Earth orbit (LEO), atmospheric drag can greatly affect the along-track drift of the formation. Leonard [24] first proposed the concept of spacecraft formation keeping using drag panels and discussed the feasibility of low-altitude orbits. Balaji [25] designed a simple proportional-integral-derivative controller in using a differential drag as a means of nano-satellite formation control. However, drag panels complicate satellite designs. Therefore, we propose a time-optimal aerodynamic control law for the along-track drift by changing the yaw attitude of the formation satellites.

The purpose of the current study is to develop a method of estimating the precise relative orbit and design a practical control scheme for satellite formation keeping.

To accomplish the relative orbit estimation, an EPF is designed based on the relative distance, elevation, and azimuth measurements. The formation keeping is divided into fuel-optimal triple-impulse in-plane motion control and single-impulse cross-track motion control. Besides, time-optimal aerodynamics control for along-track separation is also proposed. The performance of the presented approach is analyzed and compared in the last part of this paper.

The organization of this paper is as follows: Section 2 presents the relative dynamics equations and the general formation configuration description parameters. Section 3 gives the relative observer model and EPF algorithm. In Section 4, we analyze the configuration stability caused by the  $J_2$  perturbation and atmospheric drag. The formation keeping control mode is also presented. Section 5 gives the triple-impulse strategy for an in-plane motion and the single-impulse control for the cross-track motion. The effects of the thruster errors are also analyzed. Section 6 presents the time-optimal aerodynamic control law for the along-track drift. Simulations are illustrated, and analyses and comparisons of results are conducted in Section 7. The current paper ends with the conclusions in Section 8.

## 2. Relative motion model

### 2.1. Coordinate systems

The relative motion dynamics has been discussed in many papers. We consider two neighbor satellites flying in the Earth orbit. The inertial reference frame used is the J2000 frame. The origin of the coordinate system is the center of the Earth; the  $X_I$  axis points toward the mean equinox of J2000.0, the  $Z_I$  axis points toward the mean north celestial pole of J2000.0, and the  $Y_I$  axis completes the right-handed system. The relative reference frame used is the Hill frame. The origin of the coordinate system is placed at the center of mass of the master satellite; the  $x$  axis is aligned in the radial direction, the  $z$  axis is aligned with the angular momentum vector and the  $y$  axis completes the right-handed system (Fig. 1).

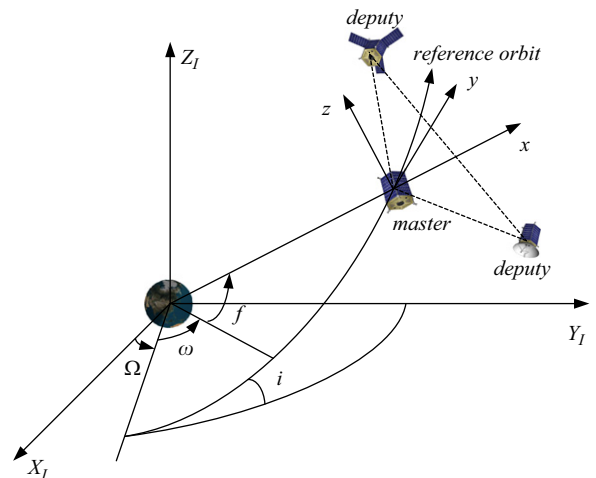


Fig. 1. J2000 inertial frame and Hill frame.

## 2.2. Description of the general formation configuration

The Keplerian orbital elements are  $a$ ,  $e$ ,  $i$ ,  $\Omega$ ,  $\omega$ , and  $u$ , which correspond to the semi-major axis, eccentricity, inclination, right ascension of the ascending node, argument of perigee, and mean argument of latitude ( $u = \omega + M$ , where  $M$  is the mean anomaly, and can be obtained from the true anomaly  $f$ ), respectively. Spacecraft-1 is the master satellite, and Spacecraft-2 is the deputy satellite. For near-circular satellite orbits, the relative eccentricity vector can be defined as follows:

$$\Delta \mathbf{e} = \begin{bmatrix} \Delta e_x \\ \Delta e_y \end{bmatrix} = \delta e \begin{bmatrix} \cos \theta \\ \sin \theta \end{bmatrix} = e_2 \begin{bmatrix} \cos \omega_2 \\ \sin \omega_2 \end{bmatrix} - e_1 \begin{bmatrix} \cos \omega_1 \\ \sin \omega_1 \end{bmatrix} \quad (1)$$

where  $\delta e$  represents the amplitude of  $\Delta \mathbf{e}$  and  $\theta$  defines the initial phase angle of the in-plane motion.

The inclination vector  $\Delta \mathbf{i}$  can be defined using the law of sines and cosines for the spherical triangle

$$\Delta \mathbf{i} = \begin{bmatrix} \Delta i_x \\ \Delta i_y \end{bmatrix} = \delta i \begin{bmatrix} \cos \varphi \\ \sin \varphi \end{bmatrix} \approx \begin{bmatrix} \Delta i \\ \Delta \Omega \sin i_1 \end{bmatrix} \quad (2)$$

where  $\Delta i = i_2 - i_1$ ,  $\Delta \Omega = \Omega_2 - \Omega_1$ ,  $\delta i$  represents the amplitude of  $\Delta \mathbf{i}$ , and  $\varphi$  defines the initial phase angle of the cross-track plane motion.

For a near-circular reference orbit, the relative motion of the formation flying satellites can be described by the following equation [26]:

$$\begin{cases} x = \Delta a - p \cos(u - \theta) \\ y = 2p \sin(u - \theta) + l \\ z = s \sin(u - \varphi) \end{cases} \quad (3)$$

where  $\{p, s, \alpha, \theta, l\}$  are the five general formation configuration description parameters;  $p = a\delta e$  represents the semi-minor axis of the relative in-plane ellipse;  $s = a\delta i$  denotes the cross-track amplitude;  $\alpha = \theta - \varphi$  defines the relative initial phase angle between the in-plane and cross-track plane motions; and  $\theta$  is the initial phase angle of the in-plane motion.  $\Delta u = u_2 - u_1$ ,  $l = a(\Delta u + \Delta \Omega \cos i) - \frac{3}{2}(u - u_0)\Delta a$ ,  $u_0$  is the initial mean argument of latitude of the deputy satellite, and  $l$  represents the along-track offset of the center of the in-plane motion. An example trajectory is shown in Fig. 2.

## 3. Relative orbit estimation based on EPF

### 3.1. Measurement model

Formation flying satellites often operate in close proximity. Their relative measuring instruments include laser range finders and radio-frequency, infrared, and visible measurements. In the current work, we adopt the laser

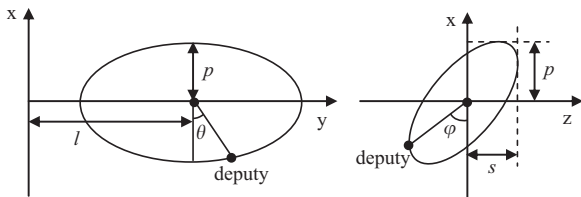


Fig. 2. Example of a relative motion in a near-circular reference orbit.

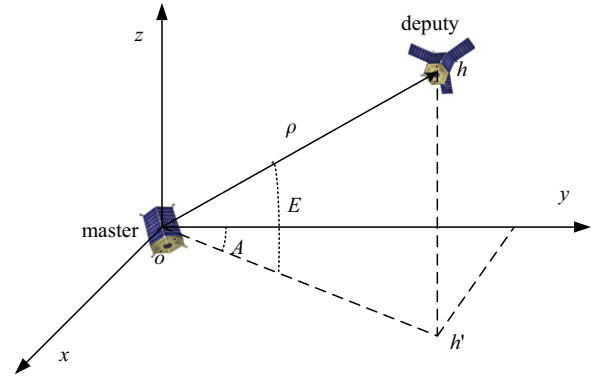


Fig. 3. Relative measurement geometry.

range finder and radio-frequency ranging equipment as the relative measurements. Thus, the high-precision relative distance, elevation, and azimuth angles can be obtained. The relative range error is zero-mean, white, Gaussian random processes having standard deviations of 0.1 m. The relative angle error is also assumed as uncorrelated Gaussian white noise processes with deviations of  $0.01^\circ$ .

The measurement geometry is shown in Fig. 3.

The relative range  $\rho$ , the azimuth angle  $A$ , and the elevation angle  $E$  can be calculated according to the following equation:

$$\mathbf{h}(\mathbf{x}) = \begin{bmatrix} \rho \\ A \\ E \end{bmatrix} = \begin{bmatrix} \sqrt{x^2 + y^2 + z^2} \\ \arctan(x/y) \\ \arcsin(z/\sqrt{x^2 + y^2 + z^2}) \end{bmatrix} \quad (4)$$

where  $\mathbf{h}(\mathbf{x})$  is the measurement matrix, and  $x$ ,  $y$ , and  $z$  are the coordinates of the deputy satellite in the body-fixed frame of the master satellite. As we know, the transformation matrix between the body-fixed frame and the Hill frame is a function of the attitude of the master satellite. In this paper, the attitude determination problem was not considered. Therefore, the relative measurements are defined with respect to the Hill frame.

The state and measurement equations can be established as follows:

$$\begin{aligned} \mathbf{X}_k &= \mathbf{f}(\mathbf{X}_{k-1}, t_k) + \mathbf{W}_k \\ \mathbf{Y}_k &= \mathbf{h}(\mathbf{X}_k, t_k) + \mathbf{V}_k \end{aligned} \quad (5)$$

where  $\mathbf{X}_k$  is the relative state vector in the Hill frame at time  $t_k$ ;  $\mathbf{Y}_k$  is the relative measurements at time  $t_k$ , which can be obtained using Eq. (4);  $\mathbf{W}_k$  is the zero mean value white Gaussian process noise with the covariance  $\mathbf{Q}_k$ ; and  $\mathbf{V}_k$  is the zero mean value white Gaussian observation noise with the covariance  $\mathbf{R}_k$ .

Five typical measurement errors, namely, the relative range and angle measurement error, the absolute position and velocity measurement error, and the attitude determination error, are considered.

### 3.2. EPF algorithm

The Kalman filter is the most common method of relative navigation. However, the PF shows better performance in a nonlinear relative state and measurement

equations. The principle of PF is to implement the recursive Bayesian filter using Monte Carlo simulations, in which the choice of the importance density function is very important [27]. We employ EKF to realize the importance sampling, which not only makes full use of the latest measurement information, but also avoids the particle exhaustion problem. The particle weights, which are closely associated with the observation, increase, whereas the other particle weights decrease.

The EPF algorithm is summarized as follows: the variable  $p(x_0)$  is the prior probability density;  $\hat{x}_{k/k-1}$  and  $\hat{x}_{k/k}$  are the predicted and updated estimates of the states at time  $t_k$ , respectively;  $P_{k/k-1}$  and  $P_{k/k}$  are their error covariance matrices, respectively;  $\Phi_{k,k-1}$  is the state transition matrix,  $K_k$  represents the Kalman gain matrix; and  $w_k^i$  represents the importance weight. The Jacobian matrix  $H_k$  is defined as follows:

$$H_k = \left. \frac{\partial h(\mathbf{X}_k, t_k)}{\partial \mathbf{X}_k} \right|_{\hat{x}_{k/k-1}} \quad (6)$$

we initialize the particles using

$$x_0^i \sim p(x_0), w_0^i = 1/N \quad i = 1, 2, \dots, N$$

Importance sampling:

- (a) The particles are updated using the following equations:

$$\begin{aligned} \hat{x}_{k/k-1} &= \Phi_{k,k-1} \hat{x}_{k-1/k-1} + Q_{k-1} \\ P_{k/k-1} &= \Phi_{k,k-1} P_{k-1/k-1} \Phi_{k,k-1}^T + Q_{k-1} \\ K_k &= P_{k/k-1} H_k^T [H_k P_{k/k-1} H_k^T + R_k]^{-1} \\ \hat{x}_{k/k} &= \hat{x}_{k/k-1} + K_k [\bar{y}_k - H_k \hat{x}_{k/k-1}] \\ P_{k/k} &= [I - K_k H_k] P_{k/k-1} \end{aligned}$$

$$\hat{x}_k^i \sim q(x_k | x_{0:k-1}^i, y_{1:k}) = N(\bar{x}_k^i, P_k^i) \quad i = 1, 2, \dots, N$$

- (b) The importance weights are calculated using the following equations:

$$w_k^i = \tilde{w}_{k-1}^i p(y_k | \hat{x}_k^i) p(\hat{x}_k^i | \hat{x}_{k-1}^i) / q(\hat{x}_k^i | x_{0:k-1}^i, y_{1:k})$$

$$\tilde{w}_k^i = w_k^i / \sum_{i=1}^N w_k^i \quad i = 1, 2, \dots, N$$

Re-sampling is conducted using

$$\{\hat{x}_{k/k}^i, w_k^i\} \rightarrow \{\hat{x}_{k/k}^i, 1/N_k\} \quad i = 1, 2, \dots, N$$

thus, the state update is expressed as follows:

$$\hat{x}_k = \sum_{i=1}^N w_k^i \hat{x}_k^i \quad i = 1, 2, \dots, N$$

## 4. Formation keeping control scheme

### 4.1. Formation stability analysis caused by the perturbations

The J2 perturbation and atmospheric drag are the main perturbations experienced by satellite formations in LEO. For a near-circular orbit, when the short periodic

perturbations are ignored, the relative eccentricity vector rotates in the e-vector plane with an angular velocity expressed by

$$\dot{\theta} \approx \frac{3}{2} (\pi/T) (R_e^2/a^2) J_2 (5\cos^2 i - 1) \quad (7)$$

where  $T$  is the orbit period.

Fig. 4 shows the in-plane relative motion that considers the J2 perturbation in a five-day evolution.

As seen in Fig. 4, the J2 perturbation does not affect the amplitude of the in-plane motion. However, Eq. (7) shows that the J2 perturbation influences the in-plane phase angle. For sun-synchronous formations at altitudes of 500 km, the in-plane phase angle  $\theta$  decreases by  $3.5^\circ$  per day.

The influences of the J2 perturbation on the relative inclination vector are described as follows:

$$\Delta \mathbf{i} = \begin{Bmatrix} \Delta i \\ \Delta \Omega \cdot \sin i \end{Bmatrix} = \begin{Bmatrix} \Delta i_x \\ \Delta i_y + \frac{d\Delta i_y}{dt} \cdot t \end{Bmatrix} \quad (8)$$

where

$$\frac{d\Delta i_y}{dt} \approx \frac{3\pi}{T} (R_e^2/a^2) J_2 \sin^2 i \times \Delta i \quad (9)$$

Eq. (9) shows that  $\Delta i$  determines the changes in the relative inclination vector. The J2 perturbation does not affect the relative inclination vector of formations with the same inclinations. Therefore, the nominal formation with  $\alpha=0^\circ$  is destroyed by the J2 perturbation, and  $\alpha=\theta-\varphi$  decreases by  $3.5^\circ$  per day. Fig. 5 shows the cross-track motion that considers the J2 perturbation in a five-day evolution.

Fig. 5 shows a slight change in the cross-track motion amplitude. However, the J2 perturbation affects the in-plane phase angle, thereby decreasing the minimum distance in the cross-track plane from 350.0 to 309.3 m. This diminishing distance affects formation safety.

The formula used to calculate the along-track drift is expressed as follows:

$$\begin{aligned} du &= (\omega_2 + M_2) - (\omega_1 + M_1) + \Delta \Omega \cos i \\ &= (\omega_2 - \omega_1) + (M_2 - M_1) + \Delta \Omega \cos i \end{aligned} \quad (10)$$

By differentiating Eq. (10), we obtain

$$du/dt = (d\omega_2/dt - d\omega_1/dt) + (dM_2/dt - dM_1/dt) + \frac{d\Delta i_y}{dt} \frac{\cos i}{\sin i}$$

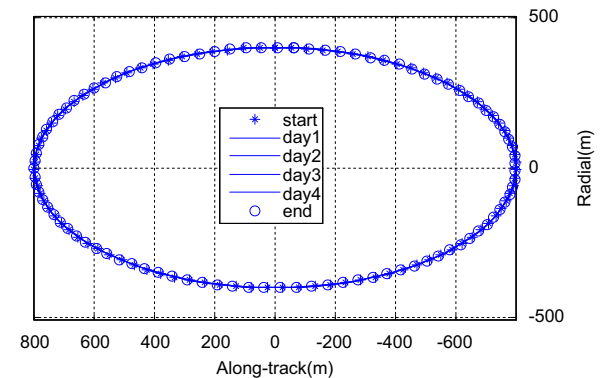


Fig. 4. In-plane motion caused by the J2 perturbation.

$$\approx -\frac{15\pi}{T}J_2(R_E^2/a^2)\cos i \sin i \Delta i - \frac{9\pi}{T}J_2(R_E^2/a^2)\cos i \sin i \Delta i$$

$$+ \frac{3\pi}{T}J_2(R_E^2/a^2)\cos i \sin i \cdot \Delta i$$

$$= -\frac{21\pi}{T}J_2(R_E^2/a^2)\cos i \sin i \Delta i \quad (11)$$

Eq. (11) shows that  $\Delta i$  determines the influences of the J2 perturbation on the along-track drift. The J2 perturbation does not affect the along-track drift of formations with the same inclinations. As discussed in Section 2, the along-track drift  $l$  and  $\Delta a$  have the following relationship per orbit:  $l = -3\pi \Delta a$ . Thus, we can offset  $\Delta a$  to compensate for the along-track drift according to Eq. (11), and the following equation is obtained:

$$\Delta a = -7J_2(R_E^2/a)\cos i \sin i \Delta i = \frac{-7J_2R_E^2}{2a}\sin(2i)\Delta i \quad (12)$$

The atmospheric drag force is much smaller than the J2 gravitational perturbation in LEO. Atmospheric drag is usually ignored in short time analyses. However, the atmospheric drag force is non-conservative, thereby yielding semi-major axis differences and causing an along-track drift. Thus, for long-period formation flying missions, the effects of the atmospheric drag must be considered during the mission design process.

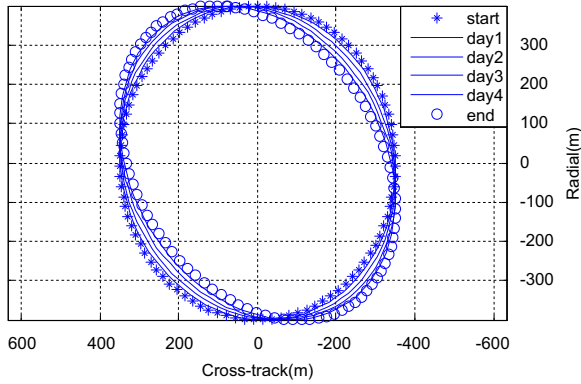


Fig. 5. Cross-track motion caused by the J2 perturbation.

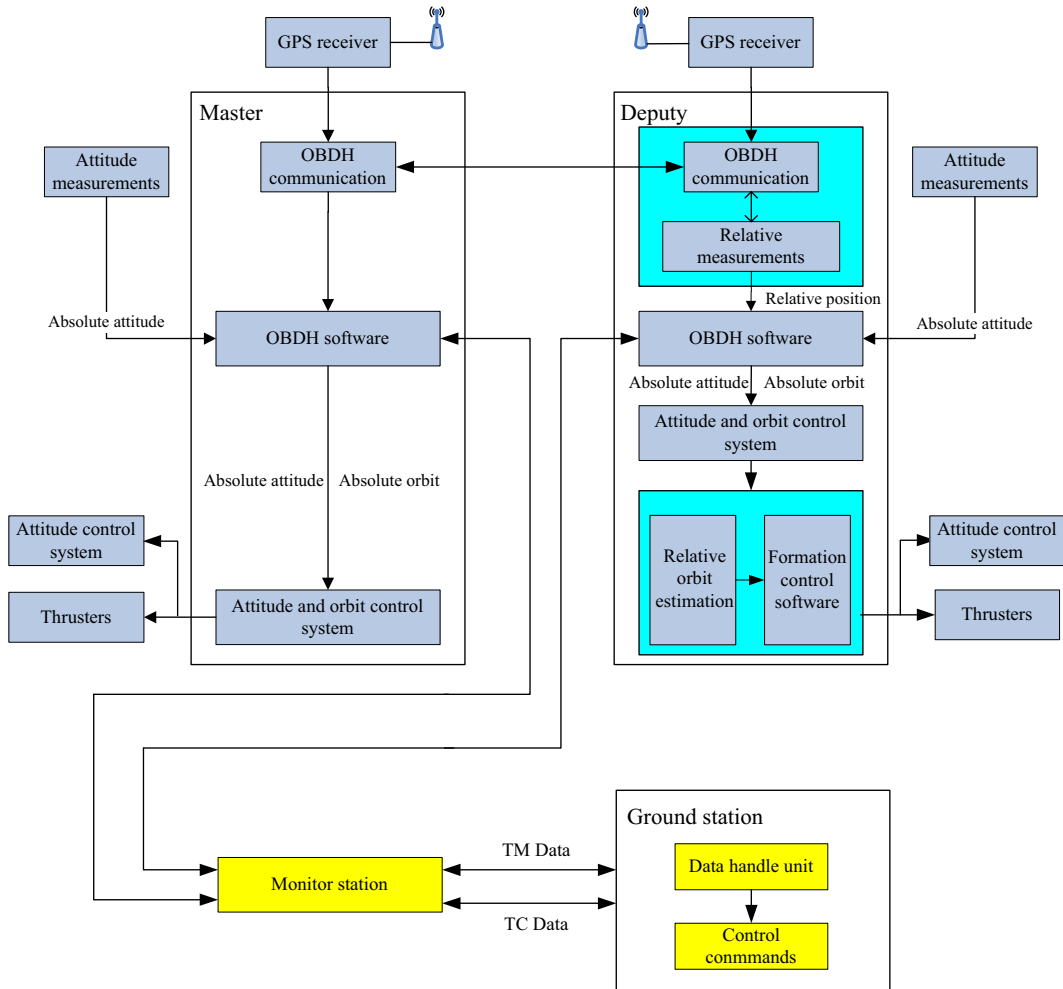


Fig. 6. Schematic diagram of the formation flying GNC system.

#### 4.2. Formation coordination control mode

We take the on-orbit TanDEM-X formation as an example. The formation configuration varies under the J2 perturbation and atmospheric drag, causing changes in the effective baseline length and formation ground coverage area [28]. Thus, maintaining the formation is necessary to accomplish the mission goals. Fig. 6 shows the schematic diagram of the formation flying guidance, navigation, and control (GNC) system. We consider an operational scenario with two formation flying satellites, and the deputy satellite performs the relative orbit correction maneuvers [29].

The deputy satellite obtains the relative measurements and performs the relative orbit estimation to obtain the high-precision relative position and velocity. The formation control software generates control commands according to the current states and mission goals. Thrusters are used to control the geometry and phase angle of the formation, and the yaw angle maneuver commands are used to control the along-track drift. The ground station can monitor the formation flying system in autonomous mode and generate formation control commands in the ground-in-the-loop mode.

#### 4.3. Formation keeping control strategy

Formation keeping control includes impulsive control for in-plane and cross-track plane configurations and aerodynamic control for along-track separation. The impulsive control is triggered according to the mission requirements periodically, and usually accomplishes within two or three orbits. It adopts the thrusters to correct the velocity. The aerodynamic control operates within the whole control periods. By maneuvering the yaw attitude angle, the relative aerodynamic drag force can be yielded, which saves the propellant.

### 5. Impulsive formation control

The Gauss variation equation can be simplified for a near-circular orbit as follows:

$$\begin{bmatrix} Da \\ De_x \\ De_y \\ Di_x \\ Di_y \\ Du \end{bmatrix} = \frac{1}{v} \begin{bmatrix} 0 & 2a & 0 \\ \sin u & 2\cos u & 0 \\ -\cos u & 2\sin u & 0 \\ 0 & 0 & \cos u \\ 0 & 0 & \sin u \\ 0 & (-3v/a) \cdot \Delta t & 0 \end{bmatrix} \begin{bmatrix} \Delta v_R \\ \Delta v_T \\ \Delta v_N \end{bmatrix} \quad (13)$$

where  $v$  is the orbit velocity of the master satellite,  $Da, De, Di, Du$  are the desired orbital corrections, and  $\Delta v_R, \Delta v_T$ , and  $\Delta v_N$  represent the velocity changes in the radial, along-track, and cross-track directions, respectively.

On the basis of Eq. (13), a thrust in the radial and along-track directions can affect the geometry and phase angle of the in-plane motion. Moreover, the along-track maneuver is doubly efficient. The along-track drift can only be corrected by an along-track thrust. A thrust in the cross-track direction influences the geometry and phase angle of the cross-track motion.

The relative orbit control scheme based on relative orbital elements is shown in Fig. 7.

#### 5.1. Triple-impulse in-plane control

We assume that the nominal configuration parameters in the orbital plane are  $p_1$  and  $\theta_1$ , and the current configuration parameters in the orbital plane are  $p_2$  and  $\theta_2$ . According to Eq. (3), the relative position in the orbital plane can be described as

$$\begin{cases} x = -p_2 \cos(u - \theta_2) + p_1 \cos(u - \theta_1) \\ y = 2p_2 \sin(u - \theta_2) - 2p_1 \sin(u - \theta_1) \end{cases} \quad (14)$$

which is equal to

$$\begin{cases} x = -p_0 \cos(u - \theta_0) \\ y = 2p_0 \sin(u - \theta_0) \end{cases} \quad (15)$$

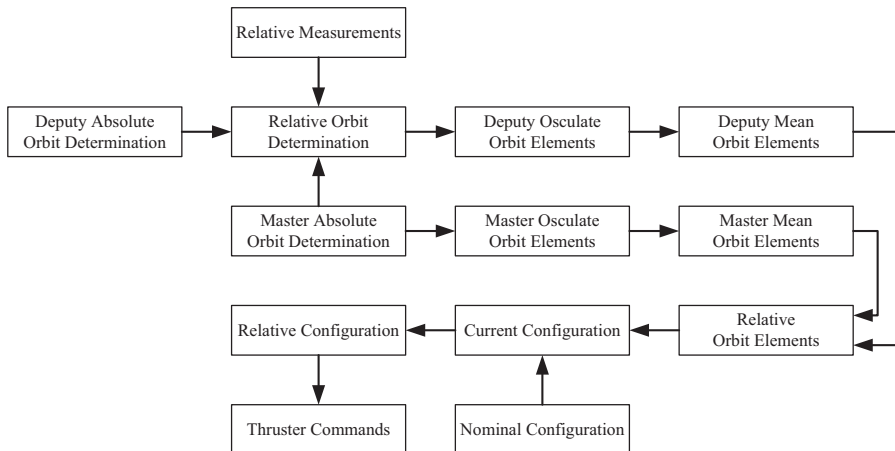


Fig. 7. Scheme of the relative orbit control.



where

$$\begin{cases} p_0 = \sqrt{p_1^2 + p_2^2 - 2p_1p_2\cos(\theta_2 - \theta_1)} \\ \varphi_0 = \arctan(p_2\sin\theta_2 - p_1\sin\theta_1, p_2\cos\theta_2 - p_1\cos\theta_1) \end{cases} \quad (16)$$

The problem of controlling the current configuration to achieve the nominal configuration is equivalent to the problem of setting  $p_0$  to zero. According to Eq. (13), the variances in the relative orbital elements can be expressed by the along-track  $\Delta v_T$

$$\begin{cases} \Delta\Delta a = (2a/v)\Delta v_T \\ \Delta\Delta l = -(3t)\Delta v_T \\ \Delta\Delta e_x = (2/v)\Delta v_T \cos u \\ \Delta\Delta e_y = (2/v)\Delta v_T \sin u \end{cases} \quad (17)$$

where  $v$  is the orbital velocity.

The relative orbital element and the configuration parameters have the following relationship:

$$\begin{bmatrix} \Delta e_{x0} \\ \Delta e_{y0} \end{bmatrix} = \frac{p_0}{a} \begin{bmatrix} \cos\theta_0 \\ \sin\theta_0 \end{bmatrix} \quad (18)$$

Setting  $p_0$  to zero is equivalent to setting  $\Delta e_{x0}$  and  $\Delta e_{y0}$  to zero. Therefore

$$\begin{cases} (2/v)\Delta v_T \cos u = -(p_0/a)\cos\theta_0 \\ (2/v)\Delta v_T \sin u = -(p_0/a)\sin\theta_0 \end{cases} \Rightarrow \begin{cases} \Delta v_T = np_0/2 \\ u = \theta_0 + \pi \end{cases} \quad (19)$$

The dual-impulse method mentioned in Refs. [18] and [20] equate to

$$\begin{cases} \Delta v_1 = \Delta v_T/2 \\ \Delta v_2 = -\Delta v_T/2 \end{cases} \quad (20)$$

The first impulse will cause an additional along-track drift during the time span between the two impulses. The influence can be neglected if the control period is small; however, if the control period is large, the influence must be considered.

The conventional dual-impulse in-plane control method causes an additional along-track drift because of the time span between the two impulses. Hence, we implement the corrections three times. The maneuver sizes are  $\Delta v_1$ ,  $\Delta v_2$ , and  $\Delta v_3$ , respectively, and the respective locations are  $u_1$ ,  $u_2$ , and  $u_3$ . The triple-impulse locations must be equal to  $\theta_0 + \pi$  or  $\theta_0$  and satisfy the following constraints:

$$\begin{cases} \Delta v_1 + \Delta v_2 + \Delta v_3 = 0 \\ |\Delta v_1| + |\Delta v_2| + |\Delta v_3| = \Delta v_T \end{cases} \quad (21)$$

We let  $u_1 = \theta_0$ ,  $u_2 = u_1 + (2k+1)\pi$ , and  $u_3 = u_2 + (2k+1)\pi$ . Thus,  $\Delta v_2 = -2\Delta v_1 = -2\Delta v_3$ .

We obtain the maneuver commands when  $u_1 = \theta_0 + \pi$ , as expressed by

$$\begin{cases} \Delta v_1 = \Delta v_T/4 \\ \Delta v_2 = -\Delta v_T/2 \\ \Delta v_3 = \Delta v_T/4 \end{cases} \quad (22)$$

and another solution when  $u_1 = \theta_0$ , as expressed by the following equation:

$$\begin{cases} \Delta v_1 = -\Delta v_T/4 \\ \Delta v_2 = \Delta v_T/2 \\ \Delta v_3 = -\Delta v_T/4 \end{cases} \quad (23)$$

The along-track drift caused by the first impulse will be compensated by the subsequent two impulses. The maneuver sizes and locations can be easily calculated according to the initial and nominal formation parameters. Eq. (19) shows that the total  $\Delta v$  needed for formation control can be calculated once the initial and nominal formation parameters are provided, which is helpful in formation-flying mission design and analysis.

## 5.2. Single-impulse out-of-plane control

The relative inclination vector of the initial and target formation configurations is  $\Delta\Delta i$ , the argument is  $\varphi_0$ , and the single burn can be provided by Eq. (13). Thus

$$\begin{cases} \Delta v_N \cos u/v = \Delta\Delta i \cos \varphi_0 = \Delta\Delta i_x \\ \Delta v_N \sin u/v = \Delta\Delta i \sin \varphi_0 = \Delta\Delta i_y \end{cases} \quad (24)$$

and

$$\begin{cases} \Delta v_N = v \|\Delta\Delta i\| \\ u = \varphi_0 = \arctan(\Delta\Delta i_y, \Delta\Delta i_x) \end{cases} \quad (25)$$

## 5.3. Thruster error model

The thruster errors include the thruster misalignment and magnitude errors, which influence the geometry and phase angle of the configuration. It is assumed that the thruster is always acting at the center of the mass of the satellite, the nominal thruster force is  $F$ , the actual thruster force is  $F^*$ , the nominal thruster direction is along the  $x$  axis of the body frame, the ratio of thruster magnitude error is  $k$ , and the thruster direction errors are  $\Delta\beta$  and  $\Delta\gamma$ , respectively. The thruster error model is shown in Fig. 8.

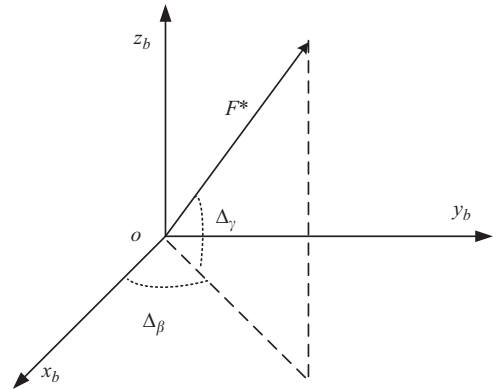


Fig. 8. Scheme of the thruster error model.

In the body frame of the satellite, the actual thruster force can be expressed as follows:

$$F^* = F(1+k) \begin{bmatrix} \cos \Delta \gamma \cos \Delta \beta \\ \cos \Delta \gamma \sin \Delta \beta \\ \sin \Delta \gamma \end{bmatrix} \quad (26)$$

Using the matrix to transform the actual thruster force in the body frame to the Hill frame, we can obtain the actual formation configuration according to Eq. (13).

## 6. Time-optimal aerodynamic control for the along-track drift

### 6.1. Relationship between the along-track drift and the cross-sectional area

The semi-major axis and orbital velocity changes have the following relationship:

$$\frac{\partial a}{\partial v} = \frac{2a^2 v}{\mu} \quad (27)$$

where  $a$  is the semi-major axis and  $v$  is the orbital velocity. Therefore

$$\frac{da}{dt} = \frac{\partial a}{\partial v} \frac{dv}{dt} = \frac{2a^2 v}{\mu} \frac{dv}{dt} \quad (28)$$

The atmospheric drag acceleration is

$$\frac{dv}{dt} = -\frac{A}{m} C_d \rho \frac{v^2}{2} \quad (29)$$

where  $m$  is the satellite mass,  $A$  is the cross-sectional area,  $C_d$  is the drag coefficient, and  $\rho$  is the atmospheric density.

Therefore, we can obtain the following equation:

$$\frac{da}{dt} = -\frac{A}{m} C_d \rho a^2 n \quad (30)$$

The differences in the cross-sectional area of the formation satellites yield the relative semi-major axis  $\Delta a$ . The cross-sectional area and  $\Delta a$  have the following relationship:

$$\Delta \dot{a} = C_d \rho a^2 n \left( \frac{A_1 - A_2}{m} \right) \quad (31)$$

where  $A_1$  and  $A_2$  represent the cross-sectional area of the master and deputy satellites, respectively.

For near-circular orbits, the along-track drift is  $\dot{l} = -\frac{3n}{2} \Delta a$ . Therefore, the relationship between the along-track drift and the cross-sectional area can be expressed as follows:

$$\ddot{l} = \frac{3}{2} n C_d \rho a^2 n \left( \frac{A_2 - A_1}{m} \right) \quad (32)$$

### 6.2. Time-optimal aerodynamic control law

For formation flying satellites, the differential drag acceleration can be caused by a difference in the relative cross-sectional area. In the current study, we maneuver the satellite yaw attitude to change the relative cross-sectional area instead of using deployable drag panels. Assuming that the nominal cross-sectional area is  $A$ , and the maneuvering yaw angle is  $\Psi$ , then the current cross-sectional area is  $A \cos \Psi$ .

The states are the along-track drift  $l$  and  $\Delta a$ , the control input is the relative cross-sectional area  $(A_2 - A_1)$ , and the time-optimal control law is adopted.

We let

$$\begin{cases} x_1 = l \\ x_2 = -\frac{3n}{2} \Delta a \\ u = \frac{3}{2} n C_d \rho a^2 n \left( \frac{A_2 - A_1}{m} \right) \end{cases} \quad (33)$$

so that

$$\begin{cases} \dot{x}_1 = x_2 \\ \dot{x}_2 = u \end{cases} \quad (34)$$

Fig. 9 shows the schematic diagram of the second-order system.

As seen in Fig. 9,  $M$  represents the excess control authority. The expressions of  $F(x_2)$  are as follows:

$$\begin{cases} F(x_2) = \frac{1}{2} \frac{x_2^2}{M} & x_2 \leq 0 \\ F(x_2) = -\frac{1}{2} \frac{x_2^2}{M} & x_2 > 0 \end{cases} \quad (35)$$

By letting  $\sigma = x_1 - F(x_2)$ , we obtain the following control laws:

$$\begin{cases} u = M & \sigma < 0 \text{ or } \sigma = 0, x_2 \leq 0 \\ u = -M & \sigma > 0 \text{ or } \sigma = 0, x_2 > 0 \end{cases} \quad (36)$$

The control system shown in Fig. 9 is a real-time closed-loop system. For the ground-in-the-loop control mode, the control commands should first be calculated and then transmitted to the satellite. Thus, the maneuver size and switching time for the implementation of the optimal control law should also be calculated first. The phase plane is shown in Fig. 10.

As shown in Fig. 10, assuming that the initial state is  $(x_{20}, x_{10})$ , the control input can be any of two cases depending on the different locations of the initial states. One case is

$$\begin{cases} t_1 = 0 & u = M \\ t_2 = \sqrt{\frac{1}{2} \left( \frac{x_{20}}{M} \right)^2 - \frac{x_{10}}{M}} & u = -M \\ t_3 = 2\sqrt{\frac{1}{2} \left( \frac{x_{20}}{M} \right)^2 - \frac{x_{10}}{M}} & u = 0 \end{cases} \quad (37)$$

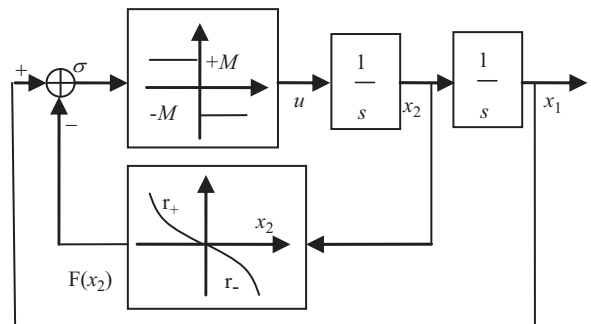


Fig. 9. Schematic diagram of the time-optimal control system for a second-order system.



and the other is

$$\begin{cases} t_1 = 0 & u = -M \\ t_2 = \sqrt{\frac{1}{2}(\frac{x_{20}}{M})^2 + \frac{x_{10}}{M} + \frac{x_{20}}{M}} & u = M \\ t_3 = 2\sqrt{\frac{1}{2}(\frac{x_{20}}{M})^2 + \frac{x_{10}}{M} + \frac{x_{20}}{M}} & u = 0 \end{cases} \quad (38)$$

Uncertainties, such as the atmospheric density estimation error, the state measurements errors, and the differences in the cross-sectional area, lead to the error in the terminal states. By letting the real control be  $\bar{M}$ , the real

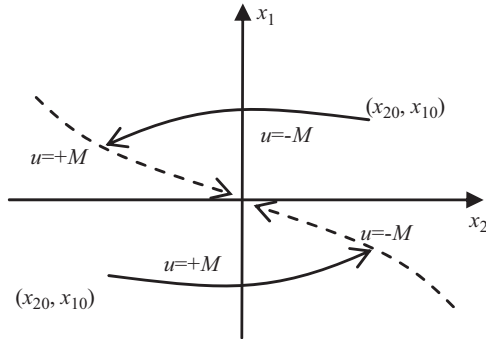


Fig. 10. Phase plane of the optimal control law for second-order system.

**Table 1**  
Mean orbital elements of the master and deputy satellites.

Elements	Master	Deputy
$a$ (m)	6892937.0	6892937.0
$e$	0.001170	0.001112
$i$ (deg.)	97.443823	97.443823
$\Omega$ (deg.)	100.0	99.997066
$\omega$ (deg.)	90.0	89.999620
$M$ (deg.)	0.0	0.0

states are  $\bar{x}_{10}$  and  $\bar{x}_{20}$ . Thus, the convergence states are

$$\begin{cases} x_{1end} = \bar{x}_{10} \left(1 - \frac{\bar{M}}{M}\right) + \left(\bar{x}_{20} - \frac{\bar{M}}{M}x_{20}\right)t_3 \\ x_{2end} = \bar{x}_{20} - \frac{\bar{M}}{M}x_{20} \end{cases} \quad (39)$$

As seen in Eq. (39), if the uncertainties are bounded, the terminal states satisfy the precision index; that is, the robustness of the optimal control law can be guaranteed.

## 7. Numerical simulations and results analysis

This section presents several numerical simulations to illustrate the performance of our approach for relative orbit estimation and control. Firstly, the EPF algorithm is verified. Then, the triple-impulse in-plane control and the conventional dual-impulse in-plane control are simulated, respectively, which demonstrate the advantages of the proposed triple-impulse in-plane control method. Finally, the aerodynamic control simulation for along-track separation is implemented in high, normal, and low solar activity periods, respectively.

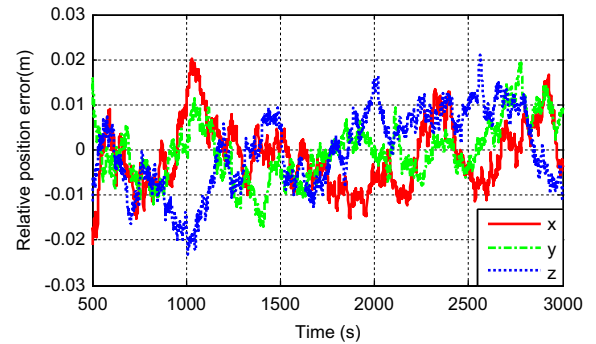


Fig. 12. Relative position estimation errors.

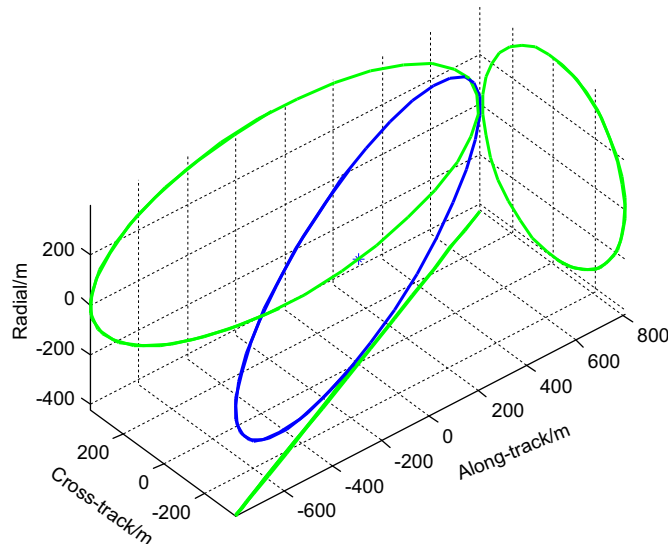


Fig. 11. Three-dimensional formation configuration.

### 7.1. Relative orbit estimation

A numerical simulation is conducted to verify the effectiveness of the presented EPF algorithm. The

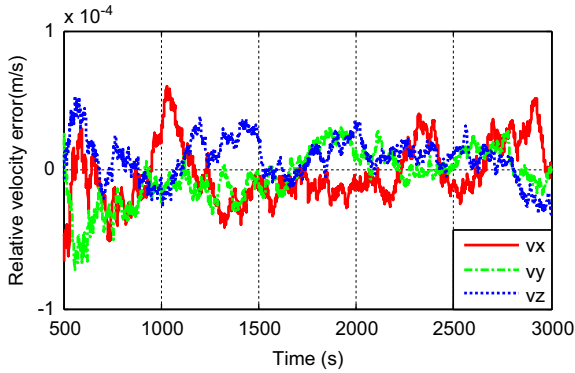


Fig. 13. Relative velocity estimation errors.

simulation conditions are as follows: the mean orbital elements of the master and deputy satellites are as shown in Table 1, and Fig. 11 shows the three-dimensional formation configuration. The formation configuration parameters are  $p=400$  m,  $s=350$  m,  $\alpha=0^\circ$ ,  $\theta=90^\circ$ ,  $l=0$  m. The absolute position and velocity measurement precision are 10 m and 0.1 m/s, respectively; and the relative range and angle measurement precision are 0.1 m and  $0.01^\circ$ , respectively. The sampling interval is 1 s. Perturbations of Earth oblateness, atmospheric drag, solar radiation pressure, perturbation of the third-body of the sun and moon, and perturbation of the Earth body tide are considered in the dynamics simulation. The fourth-order Runge–Kutta algorithm is employed for the numerical integration.

The absolute orbit of the master and deputy satellites can be generated using the Satellite Tool Kit based on the initial elements given in Table 1. The observation values can be simulated by the absolute orbit information and the measurement covariance using the Gaussian distribution

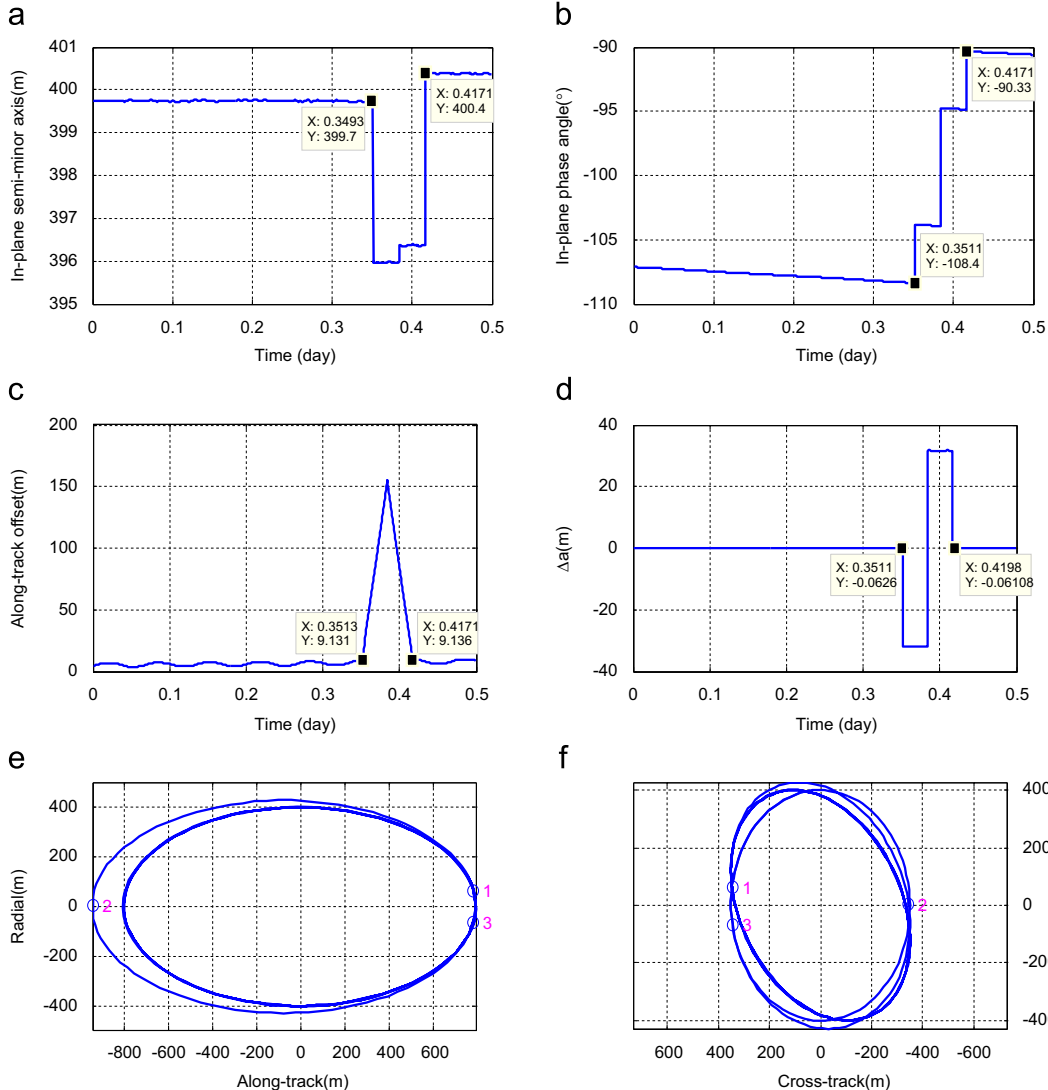


Fig. 14. Formation control using triple-impulse maneuvers. (a) In-plane geometry. (b) In-plane phase angle. (c) Along-track drift. (d) Relative semi-major axis. (e) In-plane relative motion. (f) Cross-track relative motion.

random number series. The measurement sampling period is 1 s, and the simulation time is 3000 s.

The relative position and velocity estimation errors are shown in Figs. 12 and 13, respectively.

The estimation curves are globally convergent, and the EPF algorithm achieved much faster convergence rate in the relative orbit estimation. The relative position estimation errors converge to  $2 \times 10^{-2}$  m within 500 s, and that of the relative velocity estimation are within  $1 \times 10^{-4}$  m/s. The convergence time of relative navigation for autonomous formation flying using EKF is 3000 s [30].

### 7.2. Triple-impulse in-plane control

The relative orbital elements of formation-flying satellites are shown in Table 1. The absolute position and velocity measurement precision are 10 m and 0.1 m/s, respectively; the attitude control error is  $0.1^\circ$ ; the thruster magnitude error is 1%; the relative position estimation errors are  $7.32 \times 10^{-3}$ ,  $6.42 \times 10^{-3}$ , and  $8.75 \times 10^{-3}$  m, and the relative velocity estimation errors are  $2.162 \times 10^{-5}$ ,  $1.862 \times 10^{-5}$ , and  $1.516 \times 10^{-5}$  m/s. The ratio of thruster magnitude error is 3%, and the thruster direction error is  $0.1^\circ$ . The control period is five days. Fig. 14 only shows the control process curves to present the triple impulse more clearly. The initial states are the perturbed states after a 5-d evolution. The perturbations considered and the numerical integration methods are the same as those mentioned in Section 7.1.

As seen in Fig. 14, the in-plane geometry and phase angle are corrected by the triple impulse, and the geometry slightly varies. The phase angle is corrected from  $-108.4^\circ$  to  $-90.33^\circ$ ; the along-track drift values are 9.131 and 9.136 m before and after the maneuver, respectively; and the relative semi-major axes are  $-0.0626$  and  $-0.06108$  m before and after the maneuver, respectively. The three circles in Fig. 14(e) and (f) denote the maneuver positions. Fig. 14 shows the efficiency of the triple-impulse strategy, whose main advantage is the absence of additional along-track drift. Fig. 15 shows the curves of the conventional dual-impulse maneuver.

The along-track drift values are 9.151 and 304.3 m before and after the maneuver, respectively. The conventional dual-impulse maneuver causes a large along-track

drift during the half-orbit period. Therefore, the additional along-track drift must be corrected by other along-track maneuvers, which consume more propellant.

### 7.3. Aerodynamic control for the along-track drift

We assume that the initial along-track drift is 100 m, the relative semi-major axis is  $-1$  m, the maximum yaw angle for the high and normal solar activity periods is  $4^\circ$ , and the maximum yaw angle for the low solar activity period is  $8^\circ$ . The high-fidelity simulation environment mentioned in Section 7.1 was used to test the functionality of the controller. The Jacchia70 atmospheric density

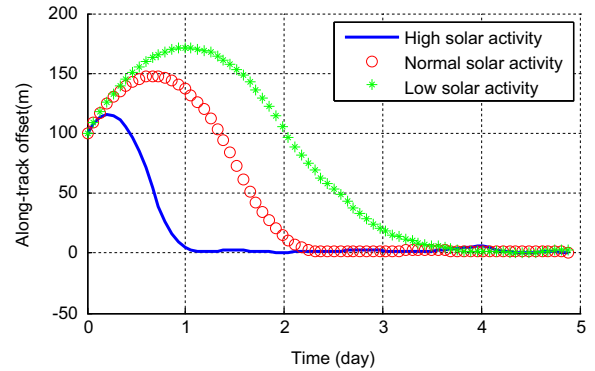


Fig. 16. Curves of the along-track drift.

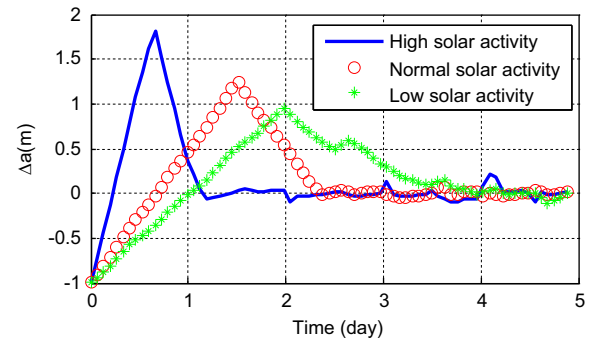


Fig. 17. Curves of the relative semi-major axis.

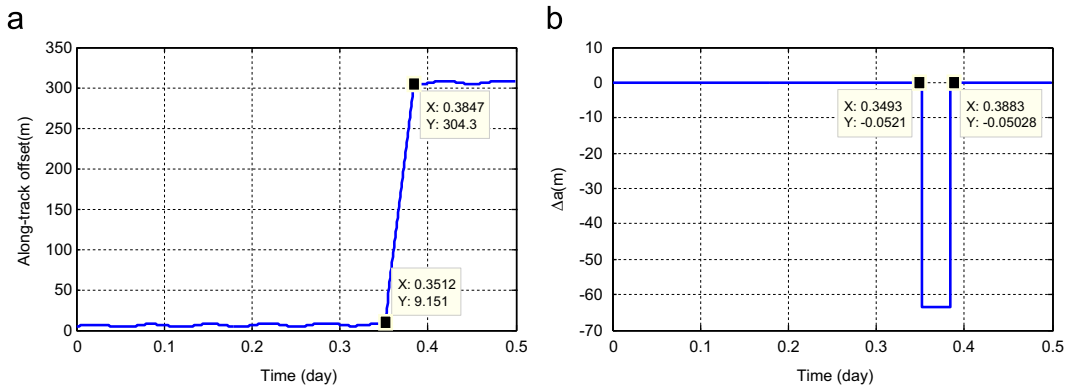


Fig. 15. Formation control using a dual-impulse maneuver. (a) Along-track drift. (b) Relative semi-major axis.

model and EGM96 Earth's gravity field model are adopted. The control period is 0.5 d. Fig. 16 shows the curves of the along-track drift, and Fig. 17 shows the curves of the relative semi-major axis.

As shown in Fig. 16, the along-track drift can have a converge within 50 m in 0.6, 1.6, and 2.6 d in high, normal, and low solar activity periods, respectively.

## 8. Conclusions

In the current paper, EPF was designed for relative orbit estimation, and the formation stability was analyzed by considering the J2 perturbation and atmospheric drag. A triple-impulse in-plane control strategy, whose analytical solutions were derived, was proposed to avoid causing additional along-track drifts. The proposed strategy is simple and convenient for onboard application. The thruster error model was developed for formation configuration control. Furthermore, the time-optimal aerodynamic control law for the along-track drift was presented. Simulation results show that the relative position estimation errors are within  $2 \times 10^{-2}$  m, the relative velocity estimation precision errors are within  $1 \times 10^{-4}$  m/s, and the precision of the along-track aerodynamic control is under 50 m.

## Acknowledgment

The authors would like to thank all the referees and editors for their valuable suggestions to improve the contents of the paper.

## References

- [1] Y.L. Zhang, G.Q. Zeng, Z.K. Wang, J.G. Hao, Theory and Application of Distributed Satellite, Science Press, Beijing, 2008 (pp. 1–2).
- [2] J.S. Ardaens, S. D'Amico, O. Montenbruck, Final commissioning of the PRISMA GPS navigation system, in: 22nd International Symposium on Spaceflight Dynamics, Sao Jose dos Campos, Brazil, 28 February–4 March, 2011, pp. 1–16.
- [3] R. Kahle, B. Schlepp, F. Meissner, M. Kirschner, R. Kiehling, TerraSAR-X/TanDEM-X formation acquisition: analysis and flight results, in: 21st AAS/AIAA Space Flight Mechanics Meeting, AAS, 13–17 February, 2011, New Orleans, Louisiana, pp. 11–245.
- [4] Y.H. Wu, X.B. Cao, Y.J. Xing, P.F. Zheng, S.J. Zhang, Relative motion coupled control for formation flying spacecraft via convex optimization, *Aerosp. Sci. Technol.* 14 (2010) 415–428.
- [5] Y.H. Wu, X.B. Cao, Y.J. Xing, P.F. Zheng, S.J. Zhang, Relative motion integrated coupled control for spacecraft formation using Gauss Pseudospectral method, *Trans. Jpn. Soc. Aeronaut. Space Sci.* 52 (2009) 125–134.
- [6] J.P. How, M. Tillerson, Analysis of the impact of sensor noise on formation flying control, in: Proceedings of the American Control Conference, 25–27 June, 2001, Arlington, VA, pp. 3986–3991.
- [7] J.F. Liu, S.Y. Rong, N.G. Cui, The determination of relative orbit for formation flying subject to J2, *Aircr. Eng. Aerosp. Technol.: Int. J.* 80 (5) (2008) 549–552.
- [8] Y.J. Xing, X.B. Cao, S.J. Zhang, H.B. Guo, F. Wang, Relative position and attitude estimation for satellite formation with coupled translational and rotational dynamics, *Acta Astronautica* 67 (2010) 455–467.
- [9] Z.H. Dang, Y.L. Zhang, Relative position and attitude estimation for Inner-Formation Gravity Measurement Satellite System, *Acta Astronautica* 69 (2011) 514–525.
- [10] G.G. Rigatos, Particle filtering for state estimation in nonlinear industrial systems, *IEEE Trans. Instrum. Meas.* 58 (11) (2009) 3885–3900.
- [11] G.H. Li, Y.A. Li, H. Yang, L. Cui, Improved unscented Kalman particle filter, in: Proceedings of the 2010 IEEE International Conference on Mechatronics and Automation, August 4–7, 2010, Xi'an, China, pp. 804–808.
- [12] D.C. Redding, N.J. Adams, E.T. Kubiak, Linear-quadratic station keeping for the STS orbiter, *J. Guidance Control Dyn.* 12 (2) (1989) 248–255.
- [13] Z.K. Wang, Y.L. Zhang, Design and verification of a Robust formation keeping controller, *Acta Astronautica* 61 (2007) 565–574.
- [14] H. Liu, J.F. Li, B.Y. Hexi, Sliding mode control for low-thrust Earth-orbiting spacecraft formation maneuvering, *Aerosp. Sci. Technol.* 10 (2006) 636–643.
- [15] H. Liu, J.F. Li, Terminal sliding mode control for spacecraft formation flying, *IEEE Trans. Aerosp. Electron. Syst.* 45 (3) (2009) 835–846.
- [16] Y.K. Li, Z.L. Jing, S.Q. Hu, Dynamic optimal sliding-mode control for six-DOF follow-up robust tracking of active satellite, *Acta Astronautica* 69 (2011) 559–570.
- [17] O. Montenbruck, M. Kirschner, S. D'Amico, S. Bettadpur, E/I-vector separation for safe switching of the GRACE formation, *Aerosp. Sci. Technol.* 10 (2006) 628–635.
- [18] S. D'Amico, O. Montenbruck, Proximity operations of formation-flying spacecraft using an eccentricity/inclination vector separation, *J. Guidance Control Dyn.* 29 (3) (2006) 554–563.
- [19] O. Montenbruck, R. Kahle, S. D'Amico, J.S. Ardaens, Navigation and control of the TanDEM-X formation, *J. Astronaut. Sci.* 56 (3) (2008) 341–357.
- [20] J.S. Ardaens, S. D'Amico, Spaceborne autonomous relative control system for dual satellite formations, *J. Guidance Control Dyn.* 32 (6) (2009) 1859–1870.
- [21] R. Kristiansen, P.J. Nicklasson, Spacecraft formation flying: a review and new results on state feedback control, *Acta Astronautica* 65 (2009) 1537–1552.
- [22] F. Wang, X.Q. Chen, A. Tsourdos, B. White, Y.H. Wu, Nonlinear relative position control of precise formation flying using polynomial eigenstructure assignment, *Acta Astronautica* 68 (2011) 1830–1838.
- [23] H.B. Sun, S.H. Li, S.M. Fei, A composite control scheme for 6DOF spacecraft formation control, *Acta Astronautica* 69 (2011) 595–611.
- [24] C.L. Leonard, Orbital formation-keeping with differential drag, *J. Guidance Control Dyn.* 12 (1) (1989) 108–113.
- [25] S.K. Balaji, N. Alfred, Y. Keisuke, R. Anton, Differential drag as a means of spacecraft formation control, *IEEE Trans. Aerosp. Electron. Syst.* 47 (2) (2011) 1125–1135.
- [26] M. Hu, G.Q. Zeng, Collision avoidance control for formation flying satellites, in: AIAA Guidance, Navigation, and Control Conference, AIAA, 2–5 August 2010, Toronto, Ontario, Canada, pp. 2010–7714.
- [27] M. Yang, W. Gao, A particle filter algorithm based on SSUKF, in: Proceedings of the 2010 IEEE International Conference on Information and Automation, June 20–23, 2010, Harbin, China, pp. 1857–1861.
- [28] J.X. Zhang, X.B. Cao, J.H. Wang, X.H. Lin, Configuration, orbit design of InSAR formation based on mean elements, *IEEE Trans. Aerosp. Electron. Syst.* 45 (2) (2009) 747–752.
- [29] M. Hu, G.Q. Zeng, H. Yao, Processor-in-the-loop demonstration of coordination control algorithms for distributed spacecraft, in: Proceedings of the 2010 IEEE International Conference on Information and Automation, 20–23 June, Harbin, China, pp. 1008–1011.
- [30] Y.H. Wu, X.B. Cao, D. Xue, Autonomous relative navigation for formation flying satellites, in: 1st International Symposium on Systems and Control in Aerospace and Astronautics, 19–21 January, 2006, Harbin, China, pp. 332–337.